



CHORUS

This is the accepted manuscript made available via CHORUS. The article has been published as:

Effects of field annealing on MnN/CoFeB exchange bias systems

P. Quarterman, I. Hallsteinsen, M. Dunz, M. Meinert, E. Arenholz, J. A. Borchers, and A. J. Grutter

Phys. Rev. Materials **3**, 064413 — Published 24 June 2019

DOI: [10.1103/PhysRevMaterials.3.064413](https://doi.org/10.1103/PhysRevMaterials.3.064413)

Effects of field annealing on MnN/CoFeB exchange bias systems

Authors: P. Quarterman^{1*}, I. Hallsteinsen^{2,3}, M. Dunz⁴, M. Meinert⁴, E. Arenholz², Julie A. Borchers¹, and A. J. Grutter¹,

Affiliations:

¹NIST Center for Neutron Research, National Institute of Standards and Technology, Gaithersburg, Maryland 20899, USA

²Advanced Light Source, Lawrence Berkeley National Laboratory, Berkeley, California 94720, USA

³Department of Electronic systems, Norwegian University of Science and Technology – NTNU, 7491 Trondheim, Norway

⁴Center for Spinelectronic Materials and Devices, Department of Physics, Bielefeld University, Germany

*Email: patrick.quarterman@nist.gov, Tel: (301)-975-8924

ABSTRACT:

We report the effects of nitrogen diffusion on exchange bias in MnN/CoFeB heterostructures as a function of MnN thickness and field annealing temperature. We find that competing effects occur in which high-temperature annealing enhances exchange bias in heterostructures with thick MnN through improved crystallinity, but in thinner samples this annealing ultimately eliminates the exchange bias due to nitrogen deficiency. Using polarized neutron reflectometry and magnetic x-ray spectroscopy, we directly observe increasing amounts of nitrogen migration from MnN into the underlying Ta seed layer with increased annealing temperature. In heterostructures with thin MnN layers, the resulting nitrogen deficiency becomes significant enough to alter the antiferromagnetic state before the Ta seed layer is nitrogen-saturated. Furthermore, we observe intermixing at the MnN/CoFeB interface which is attributed to the nitrogen deficiency creating vacancies in the MnN layer after annealing in a field. This

28 intermixing of Mn with Co and Fe is not believed to be the cause for loss of exchange bias when
29 the MnN layer is too thin but is instead a secondary effect due to increased vacancies after nitrogen
30 migration.

31 I. INTRODUCTION

32 Spintronic memories, which rely on the magnetic tunnel junction (MTJ) as a fundamental
33 building block, have garnered significant interest due to their potential applications in low power
34 non-volatile memory [1–4]. In a typical MTJ, one of the ferromagnetic layers is used as a reference
35 by pinning the magnetization direction using the exchange bias effect via an adjacent
36 antiferromagnet [5]. For this pinned magnetization to serve as an effective reference layer, the
37 antiferromagnetic layer must generate a large bias field with respect to the switching fields of the
38 ferromagnetic layers and remain stable through device operation temperatures. Since traditional
39 antiferromagnetic materials, such as IrMn and PtMn, contain expensive heavy metal elements,
40 antiferromagnetic alternatives without these materials are highly desirable for MTJ devices.

41 Recently, MnN has been investigated as a promising antiferromagnetic material for use in
42 MTJs [6–9]. The Θ -phase of MnN is a tetragonal variation of the NaCl structure with bulk lattice
43 parameters $a = b = 4.256 \text{ \AA}$, $c = 4.189 \text{ \AA}$ at room temperature and has a Néel temperature of
44 approximately 660 K [10–13]. Previous reports on polycrystalline MnN/CoFe structures show an
45 exchange bias field of 180 mT, a blocking temperature of 453 K, and an interfacial exchange
46 energy of $J_{eff} = 0.41 \text{ mJ/m}^2$ [6]. More recently, Dunz *et al* have shown that high temperature
47 annealing can enhance the exchange bias field to greater than 200 mT [8]. However, the optimal
48 field annealing temperature depends strongly on the MnN thickness, and when the MnN thickness
49 is below a critical thickness the high temperature annealing process destroys the exchange bias
50 effect. In this work, it was postulated that nitrogen diffusion from the MnN into underlying Ta
51 seed layers is the cause, and Auger depth profiling showed that annealing does indeed lead to
52 nitrogen migration. However, since Auger electron spectroscopy (AES) analysis is sensitive only

53 to the structural depth profile, it does not provide insight into how nitrogen diffusion affects the
54 magnetic properties and cannot explain the thickness dependence.

55 In this work, we use polarized neutron reflectometry (PNR) and x-ray magnetic circular
56 dichroism (XMCD) to develop a comprehensive understanding of the structural and magnetic
57 properties in samples with varied annealing temperature and MnN thickness. We demonstrate that
58 the MnN layer must be sufficiently thick in comparison to the underlying Ta seed layer in order to
59 maintain a robust exchange bias at high annealing temperatures. If the MnN layer is too thin
60 relative to the Ta layer, then the MnN will become heavily nitrogen deficient before the Ta layer
61 is saturated. This deficiency leads to interdiffusion with the ferromagnetic layer and suppression
62 of the MnN antiferromagnetic order at the interface, causing the desired exchange bias effect to
63 disappear.

64 II. EXPERIMENTAL METHODS

65 Thin film samples of Ta(10)/MnN(t_{MnN})/CoFeB(t_{CoFeB})/TaO_x(2.5), where the nominal
66 thicknesses are denoted in nm and $t_{MnN} = 30$ and 48 nm and $t_{CoFeB} = 1.6$ and 7 nm, were grown on
67 thermally oxidized Si/SiO₂ ($t_{SiO_2} = 50$ nm) substrates using magnetron sputtering at room
68 temperature. The MnN layer was grown under reactive conditions using a Mn target and a Ar:N₂
69 gas ratio of 1:1. Exchange bias was set in the samples by post annealing under vacuum for 15
70 minutes, followed by field cooling at 650 mT along a direction parallel to the sample plane. We
71 examined samples as-deposited (non-field annealed) and after field annealing at 325 °C and 525
72 °C. The crystallographic properties of MnN were probed using wide angle x-ray diffraction (XRD)
73 shown in supplemental Fig. 1 [14]. The magnetization (M) as a function of applied field (H)
74 properties were characterized using the longitudinal magneto-optical Kerr effect (MOKE). To
75 probe the depth dependence of the nuclear structure and in-plane component of the magnetization,

76 we measured PNR using the PBR (Polarized Beam Reflectometer) instrument at the National
77 Institute of Standards and Technology Center for Neutron Research. The incident neutron spins
78 were polarized parallel or antiparallel to H , and reflectivity was measured in the non-spin flip
79 cross-sections (R^{++} and R^{--}) as a function of the momentum transfer (Q) normal to the film surface.
80 Measurements were collected at room temperature in a saturating magnetic field of 700 mT applied
81 along the field annealing direction. PNR data were reduced and modeled using the Reductus and
82 REFL1D software packages [15,16]. X-ray absorption spectra (XAS) were measured with
83 circularly polarized x-rays and the x-ray magnetic circular dichroism (XMCD) spectra obtained as
84 difference between the XAS with antiparallel and parallel orientation of magnetization and photon
85 helicity. All spectra were measured in total-electron yield (TEY) mode on the L_2 and L_3 edges for
86 Fe, Co and Mn, using beamline 4.0.2 at the Advanced Light Source. The samples were measured
87 in the grazing incidence condition (30° from the sample plane) at room temperature switching the
88 magnetic field between ± 0.3 T.

89 III. RESULTS

90 MOKE measurements for $t_{CoFeB} = 1.6$ nm and both MnN thicknesses are shown in Fig. 1a.
91 The substrate background was removed by subtracting a linear fit to the positive high field data.
92 At the corresponding high negative field region, the magnetization does not completely saturate,
93 which may be indicative of an uncompensated, pinned moment [5]. The 30 nm MnN sample
94 shows an exchange bias field (H_{ex}) of 140 mT after 325 °C field annealing, but the exchange bias
95 disappeared after field annealing at 525 °C. A similar drop in H_B was observed in thinner MnN
96 layers at high annealing temperature. The 48 nm MnN sample, however, shows H_{ex} increased from
97 130 mT at 325 °C to 270 mT at 525 °C. Additionally, the 30 nm MnN sample showed an increased
98 coercive field (H_c) from 57 mT to 135 mT after annealing at 525 °C, while the 48 nm MnN sample

99 exhibited no noticeable increase for H_c . The exchange bias field and coercivity as a function of
 100 annealing temperature are plotted in Fig. 1b. Previously Ta/MnN/CoFe structures have been
 101 studied with AES and MOKE [8]. In these reports, AES suggested nitrogen diffusion into Ta in
 102 all samples considered upon annealing.

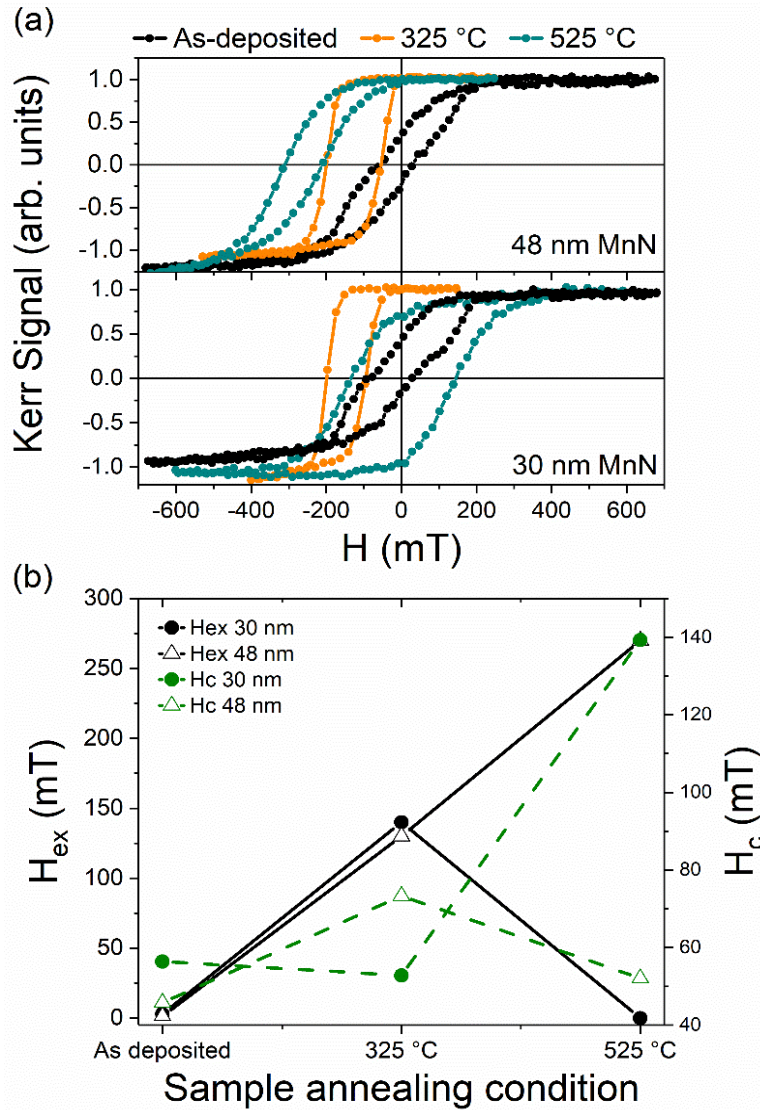


FIG. 1: (a) Normalized MOKE measured with field applied along the in-plane field-annealing axis for 1.6 nm CoFeB on 48 nm (top) and 30 nm (bottom) MnN. (b) Exchange bias field (black, solid) and coercive field (green, dashed) for the 30 nm (solid) and 48 nm (open) MnN samples with 1.6 nm CoFeB.

103

104 To further understand the role of annealing and nitrogen diffusion, PNR has been measured
105 on the 7 nm CoFeB set of samples since the technique is sensitive to both the nuclear and magnetic
106 depth profiles. We note that the PNR and MOKE measurements were performed on samples with
107 different CoFeB thicknesses (7 and 1.6 nm, respectively). In PNR, the thicker CoFeB allows for
108 magnetic effects to be more prominently observed due to the additional reflectivity oscillations
109 visible above background. Since the temperature-dependent effects are observed in both CoFeB
110 thicknesses, we expect observations to be similar for both sample sets. Further, we note that PNR
111 is particularly sensitive to nitrogen movement from MnN into Ta since the scattering length density
112 (SLD) of Mn is strongly negative while the SLD for nitrogen is strongly positive. Subsequently
113 there is a large difference between the SLD of Ta ($3.83 \times 10^{-6} \text{ \AA}^{-2}$) and TaN ($6.89 \times 10^{-6} \text{ \AA}^{-2}$).

114 PNR for the R^{++} and R^{--} scattering cross sections are shown in Fig 2 alongside theoretical
115 fits; the magnetic contribution to the scattering is highlighted by the spin asymmetry (SA) in
116 supplemental Fig. 2, where $SA = (R^{++} - R^{--}) / (R^{++} + R^{--})$. The PNR and SA show significant changes
117 in key features as the annealing temperature is increased. The SLD profiles used to generate the
118 theoretical fits can be seen in Fig. 3a and 3b for the nuclear structure and for the in-plane
119 component of the magnetization as a function of depth. In this model, the MnN layer was divided
120 into four regions, to allow for variation in the nitrogen content across the layer. Models including
121 one, two and three sublayers within the MnN layer were explored, and it was determined that four
122 sublayers were required to yield a satisfactory χ^2 and nuclear scattering length density profiles that
123 are physically meaningful. (An in-depth discussion of these simple models and resulting PNR fits
124 can be found in the supplementary information) [14]. The underlying Ta layer was separated into
125 Ta and TaN regions since AES in prior work showed interdiffusion at the Ta and MnN interface.
126 In the fitting of post-annealed samples, a boron heavy layer was allowed to form at the

127 CoFeB/TaO_x interface, as reported for CoFeB/Ta interfaces by Zhu *et al* [17]. The Ta layer shows
 128 an initial TaN layer at the Ta/MnN interface, and the Ta absorbs more nitrogen as the annealing
 129 temperature increases until it is saturated at 525 °C. Fitting the PNR data at high annealing
 130 temperatures required profiles in which ferromagnetism sweeps into the top interface of the MnN
 131 layer, suggesting an intermixing of Mn with Fe or Co. While the peak magnetic SLD in the CoFeB
 132 decreases with increased annealing temperature, the total integrated magnetic SLD increases. The
 133 resulting PNR fits capture the resulting changes in the structural and magnetic depth profile
 134 extremely well, with a χ^2 of 2.51 or better.

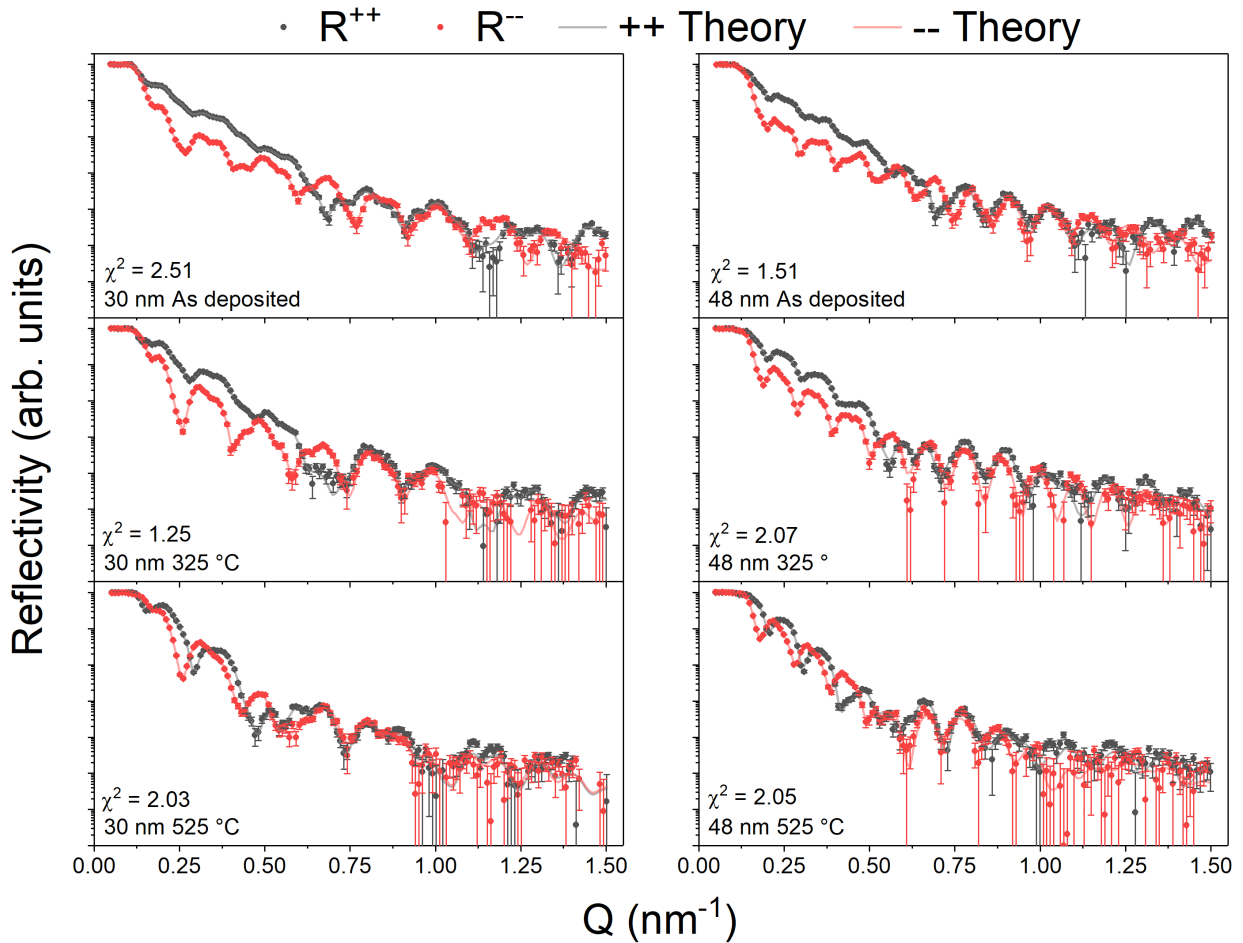


FIG. 2: The measured polarized neutron reflectivity (points) with theoretical fits (solid lines) in the non-spin flip configuration. Results are shown for the 30 and 48 nm MnN in the as-deposited state, and after annealing at 325 °C and 525 °C. Error bars are representative of 1 σ .

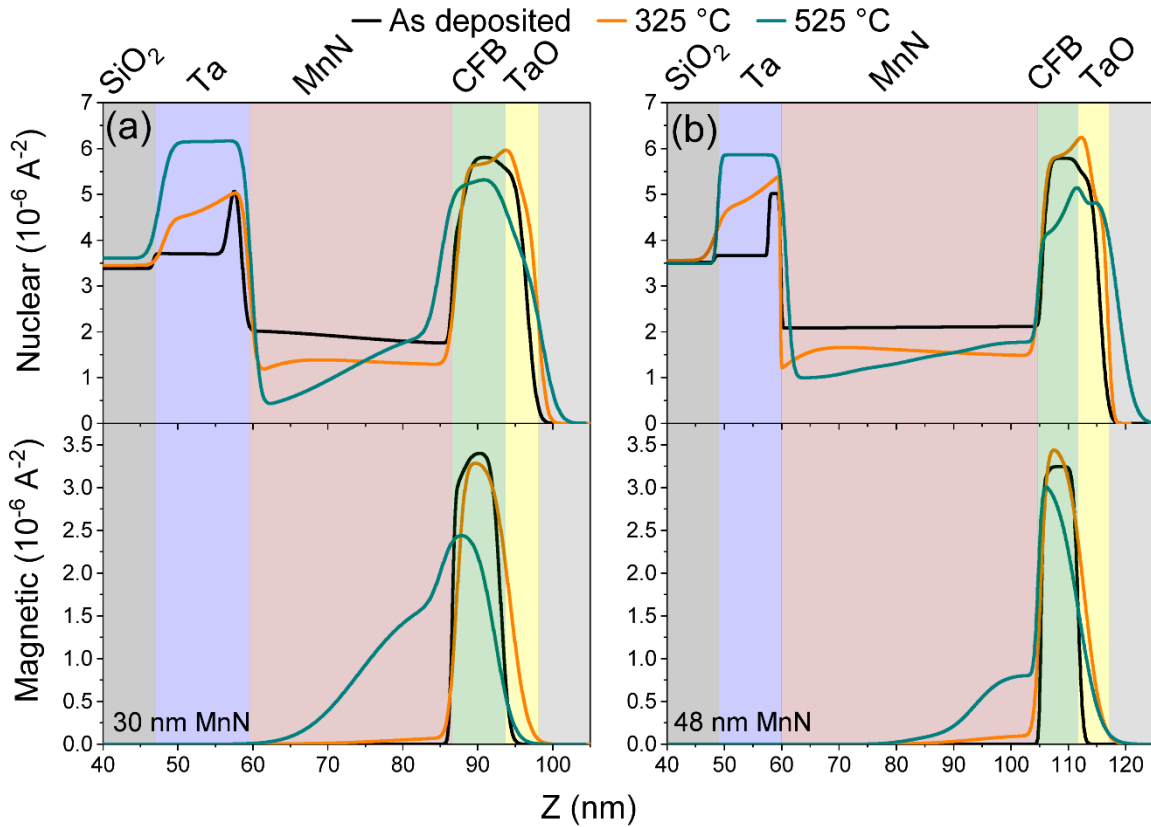


FIG. 3: Nuclear (top) and magnetic (bottom) scattering length density profiles for the 7 nm CoFeB samples with (a) 30 nm and (b) 48 nm of MnN. The layers are denoted by their nominal thicknesses and distance is referenced such that the substrate surface is at 0 nm.

137

138 In order to investigate the interfacial magnetic layer between CoFeB and MnN suggested
 139 by the PNR models, XMCD was employed on the 30 nm MnN with 7 nm CoFeB sample. XMCD
 140 for the L_2 and L_3 edges of Fe, Co and Mn are shown in Fig 4. The fine structure of the XAS shows
 141 a 2+ Mn state due to the ionic bonding of Mn with N. We observe a dramatic change in the x-ray
 142 absorption L_3 edge intensities (Fig. 4a), for Co, Fe and Mn, after annealing at 525 °C as compared
 143 to the pre-edge intensity—this normalization scheme provides the number of Fe, Co and Mn
 144 atoms. Specifically, the Fe and Co signal decreases while the Mn signal dramatically increases.
 145 Since TEY-XMCD is sensitive primarily to the top 5 nm of the samples, this result provides insight

146 into the interdiffusion process. The average x-ray absorption spectra, in Fig. 4a, from
147 measurements with antiparallel and parallel orientation of magnetization and photon helicity are
148 normalized by dividing the peak value by the pre-edge intensity to obtain the moment per
149 atom [18]. The XMCD, in Fig. 4b-d, was normalized to the maximum intensity of the averaged
150 XAS spectra and is shown as a percentage of the XAS intensity. By normalizing with this method,
151 the XMCD signals can be directly compared; the magnitude of the XMCD for Fe (Fig. 4b) and Co
152 (Fig. 4c) peaks increases with annealing temperature which indicates the magnitude of
153 magnetization increases [19]. In the case of Mn (Fig. 4d), there is a small (relative to that of Fe
154 and Co) XMCD signal in the as-deposited sample. After annealing the samples at 325 and 525 °C,
155 the Mn XMCD drops to zero. There is a small feature at the 325 °C Mn L₃ edge, however, due to
156 how small the effect is, we cannot be certain the feature is significant and not caused by drift-
157 related artifacts associated with the large intensity of the L₃ XAS edge. Furthermore, there is no
158 definitive feature of opposite sign at the L₂ edge.

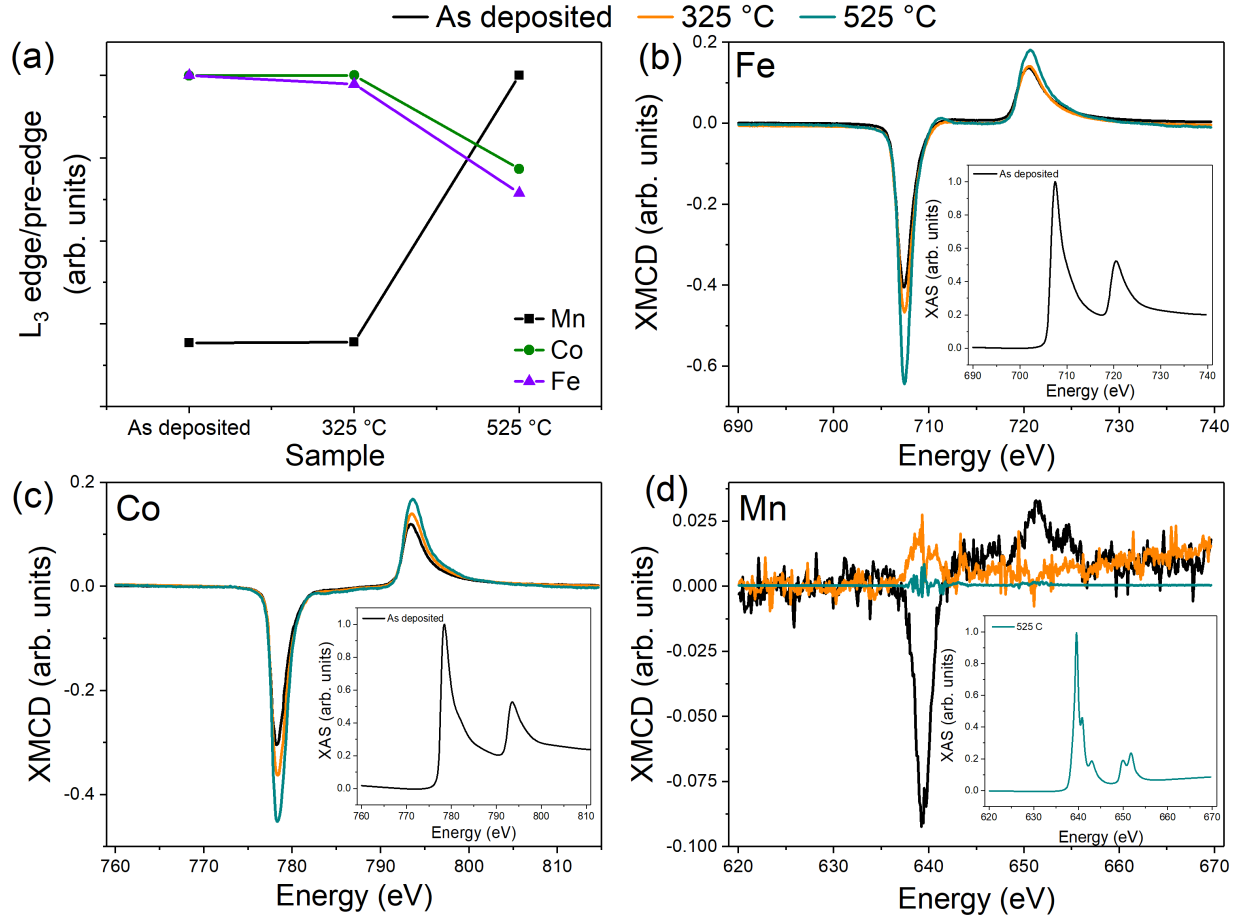


FIG. 4: XMCD and inset of XAS for (a) Fe, (b) Co, and (c) Mn with the XAS shown in the inset figures. (d) The L₃ peak intensity normalized to the pre-edge intensity as a function of annealing temperature. Data measured on the sample with 30 nm of MnN and 7 nm CoFeB

159

160 IV. DISCUSSION

161 From the PNR, XAS/XMCD, and XRD results, we can construct a comprehensive,
 162 element-specific understanding of why MnN thickness and field annealing temperature have such
 163 strong effects on MnN-based exchange bias systems. Note that XRD, shown in supplemental Fig.
 164 1, further supports the structural changes observed with PNR and demonstrates that the samples
 165 studied in this work behave similarly to those in previous reports [8,20]. PNR reveals that the
 166 MnN layer is nitrogen rich in the as-deposited samples, which manifests through a nuclear SLD
 167 ($2.09 \times 10^{-6} \text{ \AA}^{-2}$) larger than that of bulk MnN ($1.77 \times 10^{-6} \text{ \AA}^{-2}$) and an expanded lattice observed

168 by XRD (supplemental Fig. 1) [14]. We also observe that the 30 nm MnN sample appears to have
169 larger nitrogen content near the Ta interface than near the CoFeB interface, whereas this gradient
170 for the as-deposited condition is not observed in the 48 nm sample (supplemental Fig. 5). It
171 remains unclear if this difference is intrinsically due to the MnN thickness or variations in the
172 nitrogen reactive sputtering process. In the as-deposited state, XMCD reveal the presence of a
173 small ferromagnetic moment on the Mn atoms (Fig. 4d), in comparison to the observed moments
174 on Fe and Co, at the MnN/CoFeB interface, which is concluded to not be due to interdiffusion of
175 Co or Fe into the MnN. Since the Mn moment in this thin layer is small and overshadowed by the
176 strong neighboring ferromagnetic layer, it is challenging to resolve the magnetization of Mn, in
177 proximity to a strong ferromagnet like CoFeB, with PNR modeling. XMCD shows that the
178 moment on the Mn quickly disappears after annealing, as the antiferromagnetic Θ -phase is
179 stabilized into the bulk crystal structure. At the Ta/MnN interface there is an intermediate TaN
180 layer, even in the as-deposited state, which is probably created by the reactive plasma exposition
181 during the growth process. After annealing at 325 °C, nitrogen migrates from the MnN layer into
182 the underlying Ta layer, which leads to a gradient in nitrogen content across the Ta and MnN
183 layers. This nitrogen migration, which occurs in a similar fashion for both the 30 and 48 nm MnN
184 samples, causes the average nuclear SLD in the MnN and Ta layers to decrease and increase,
185 respectively. At this field annealing condition, a high nuclear SLD region at the top of the CoFeB
186 arises, which a previous PNR report by Zhu *et al.* concluded was due to boron segregating out of
187 the film [17]. Note that later electron microscopy studies by Wang *et al.* suggest the B moved into
188 interstitial sites of neighboring TaO_x layers [21]. This boron segregation is expected to yield an
189 increased magnetization in the remaining CoFe film, as was confirmed by an increase in the
190 XMCD signal for both Fe and Co L_{2,3} edges. While the magnetic scattering length density peak

191 value obtained from PNR decreases as the annealing temperature increases, the overall integrated
192 magnetic SLD (which is magnetization per depth) increases due to the migration of Fe and Co.
193 Thus, the changes in magnetic scattering length density are consistent with the increase in XMCD
194 signal, which measures magnetic moment per atom.

195 Increasing the field annealing temperature to 525 °C leads to dramatic differences between
196 the 30 nm and 48 nm MnN samples in the MOKE hysteresis loops (Fig. 1a), SLD profiles (Fig. 3)
197 and XMCD spectra (Fig. 4b, c,d). In both samples, we observe that the Ta becomes almost entirely
198 saturated with nitrogen absorbed from the MnN layer, as shown by an increase in the SLD in the
199 Ta layer which approaches the bulk TaN value ($6.8 \times 10^{-6} \text{ \AA}^{-2}$). The removal of N from MnN results
200 in intermixing of Mn with Fe and Co at the MnN/CoFeB interface; Mn in the nominal CoFeB
201 causes the nuclear SLD to decrease, whereas Co and Fe in the MnN layer results in an increased
202 nuclear SLD. We clearly see in the magnetic SLD profile that this interdiffusion also leads to
203 ferromagnetism sweeping into the MnN layer, which is attributed to the intermixing of Mn with
204 Fe and Co since the SLD near the top of the nominal MnN layer increases. However, we cannot
205 rule out the formation of iron- and cobalt-nitrides, both of which have ferromagnetic and
206 antiferromagnetic phases [22,23]. As the 30 nm MnN layer contains less nitrogen to donate, the
207 resulting nuclear SLD gradient in MnN, is far more extreme than in the case of 48 nm MnN. We
208 postulate that the more extreme case of nitrogen deficiency yields more vacancies that aid
209 interdiffusion, so that intermixing is significantly more pronounced in the 30 nm sample— shown
210 in both the nuclear and magnetic SLD profiles with the latter extending through most of the
211 nominal MnN layer (Fig. 3a). The XAS intensity (Fig 4a) also supports a picture of interdiffusion
212 at the MnN/CoFeB interface after high temperature annealing. The intensity of the L_3 edge for Fe,
213 Co and Mn is the same for the as-deposited and 325 °C annealing condition, but exhibits a sharp

214 increase in the Mn signal and decrease for Fe and Co. Since we collected the XAS and XMCD in
215 TEY mode, the data are primarily sensitive to the surface with signal contributions originating
216 deeper in the film being attenuated with a characteristic decay length of 5 nm. We therefore
217 conclude that the Fe and Co diffused deeper into the sample, while the Mn migrated towards the
218 surface, in excellent agreement with the SLD profiles.

219 The MOKE measurements show that the exchange bias is progressively enhanced by
220 increased annealing temperature for the sample with 48 nm of MnN, but the exchange bias
221 disappears at high annealing temperature when the MnN thickness is 30 nm. We surmise that the
222 30 nm MnN layer becomes so nitrogen deficient that the layer is no longer antiferromagnetic after
223 the high temperature annealing process. Since the exchange bias also disappears in the 1.6 nm
224 CoFeB sample, we conclude that interdiffusion of Co, Fe and Mn is not the cause because the
225 intermixing will be far more limited than in the 7 nm CoFeB samples. However, in the 48 nm MnN
226 sample, there is enough nitrogen remaining after the Ta layer becomes saturated with nitrogen to
227 maintain Θ -phase MnN which preserves the antiferromagnet/ferromagnet interface. Furthermore,
228 we observe that the thicker MnN sample displays an increased exchange bias field (supplemental
229 Fig. 2.) even upon annealing at 525 °C. XRD measurements (supplemental Fig. 1) conclusively
230 demonstrated that the increased annealing temperature allows for the remaining MnN to relax into
231 the bulk crystal structure with improved texture; which likely accounts for the enhanced exchange
232 bias field. However, additional studies to better understand the role that intermixing between Co,
233 Fe and Mn has on the magnetic properties are of interest. A thinner Ta layer may allow for thin
234 MnN to maintain the exchange bias effect after high temperature annealing since less nitrogen will
235 be required to saturate the layer. Alternatively, preemptively nitriding the Ta layer during

236 deposition or including a diffusion barrier may also improve the thermal stability of MnN/CoFeB
237 systems to realize even larger bias fields.

238 **V. CONCLUSIONS**

239
240 In this work, we resolve the question of thickness and annealing temperature-dependent
241 exchange bias effect in MnN/CoFeB heterostructures. PNR, XMCD, and XRD characterization
242 have been used to probe both the nuclear and magnetic structure to understand the role of nitrogen
243 diffusion in MnN-based systems. We have shown that nitrogen migrates from the initially
244 nitrogen-heavy MnN films into a neighboring Ta layer as a function of annealing temperature.
245 When there is not an adequate amount of nitrogen to maintain the stability of the entire MnN film,
246 then Co and Fe begin to diffuse into the nominal MnN layer, which can decrease, or even eliminate,
247 the exchange bias. An increase in the net magnetization of the ferromagnetic layer at high
248 annealing temperatures has also been observed, which is attributed to both the segregation of boron
249 to the top interface and intermixing with the underlying Mn heavy layer. The inclusion of a
250 diffusion barrier layer at the Ta/MnN interface, such as TaN, or a thinner seed layer may allow for
251 higher annealing temperatures to be used without degrading the MnN layer, opening the possibility
252 of even larger exchange bias fields in MnN based MTJs.

253
254 **ACKNOWLEDGEMENTS**
255 P. Q. acknowledges support from the National Research Council Research Associateship Program.
256 Research performed in part at the NIST Center for Nanoscale Science and Technology. This
257 research used resources of the Advanced Light Source, which is a DOE Office of Science User
258 Facility under contract no. DE-AC02-05CH11231. M.M. acknowledges financial support from the
259 Deutsche Forschungsgemeinschaft (DFG) under sign no. ME 4389/2-1.

260 **REFERENCES**

- 261 [1] A. V. Khvalkovskiy, D. Apalkov, S. Watts, R. Chepulsii, R. S. Beach, A. Ong, X. Tang,
262 A. Driskill-Smith, W. H. Butler, P. B. Visscher, D. Lottis, E. Chen, V. Nikitin, and M.
263 Krounbi, *J. Phys. D Appl. Phys.* **46**, 139601 (2013).
- 264 [2] K. L. Wang, J. G. Alzate, and P. Khalili Amiri, *J. Phys. D* **46**, 074003 (2013).
- 265 [3] A. Makarov, T. Windbacher, V. Sverdlov, and S. Selberherr, *Semicond. Sci. Technol.* **31**,
266 113006 (2016).
- 267 [4] T. Endoh, H. Koike, S. Ikeda, T. Hanyu, and H. Ohno, *IEEE J. Emerg. Sel. Top. Circuits*
268 *Sys.* **6**, 109 (2016).
- 269 [5] J. Nogues and I. K. Schuller, *J. Mag. Mag. Mater.* **192**, 203 (1999).
- 270 [6] M. Meinert, B. Büker, D. Graulich, and M. Dunz, *Phys. Rev. B.* **92**, 144408 (2015).
- 271 [7] P. Zilske, D. Graulich, M. Dunz, and M. Meinert, *Appl. Phys. Lett.* **110**, 192402 (2017).
- 272 [8] M. Dunz, J. Schmalhorst, and M. Meinert, *AIP Adv.* **8**, 056304 (2018).
- 273 [9] Y. Ferrante, J. Jeong, R. Saha, S. V. Faleev, M. G. Samant, T. Topuria, H. Deniz, and S.
274 S. P. Parkin, *APL Mater.* **7**, 031103 (2019).
- 275 [10] N. A. Gokcen, *Alloy Phase Diagr.* **11**, 33 (1990).
- 276 [11] K. Suzuki, T. Kaneko, H. Yoshida, Y. Obi, H. Fujimori, and H. Morita, *J. Alloy. Compd.*
277 **306**, 66 (2000).
- 278 [12] M. Tabuchi, M. Takahashi, and F. Kanamaru, *J. Alloy. Compd.* **210**, 143 (1994).
- 279 [13] Y. Yamaguchi, H. Fujimori, H. Morita, T. Kaneko, Y. Obi, K. Suzuki, and H. Yoshida, *J.*
280 *Phys. Soc. Jpn.* **70**, 1084 (2005).
- 281 [14] See supplemental material at [URL Will Be Inserted by Publisher] for XRD
282 characterization and additional analysis of the PNR and modeling. Alternative models
283 with fewer MnN sublayers are shown.
- 284 [15] B. J. Kirby, P. A. Kienzle, B. B. Maranville, N. F. Berk, J. Krycka, F. Heinrich, and C. F.
285 Majkrzak, *Curr. Opin. Colloid Interface Sci.* **17**, 44 (2012).
- 286 [16] P. A. Kienzle, B. B. Maranville, K. V. O'Donovan, J. F. Ankner, N. F. Berk, and C. F.
287 Majkrzak, <https://www.nist.gov/ncnr/reflectometry-software> (2017).
- 288 [17] T. Zhu, Y. Yang, R. C. Yu, H. Ambaye, V. Lauter, and J. Q. Xiao, *Appl. Phys. Lett.* **100**,
289 202406 (2012).
- 290 [18] W. L. O'Brien and B. P. Tonner, *Phys. Rev. B.* **50**, 672 (1990).
- 291 [19] C. Piamonteze, P. Miedema, and F. M. F. de Groot, *Phys. Rev. B.* **80**, 184410 (2009).
- 292 [20] M. Dunz, B. Büker, and M. Meinert, *J. Appl. Phys.* **124**, 203902 (2018).
- 293 [21] Z. Wang, M. Saito, K. P. McKenna, S. Fukami, H. Sato, S. Ikeda, H. Ohno, and Y.

- 294 Ikuhara, *Nano Lett.* **16**, 1530 (2016).
- 295 [22] J. M. D. Coey and P. A. I. Smith, *J. Magn. Magn. Mater.* **200**, 405 (1999).
- 296 [23] M. B. Lourenço, M. D. Carvalho, P. Fonseca, T. Gasche, G. Evans, M. Godinho, and M.
297 M. Cruz, *J. Alloy. Compd.* **612**, 176 (2014).

298

299